(Received 11 November 2024, Accepted 20 January 2025, Scheduled 3 February 2025)

Multifunctional Dual-Band Microwave Sensor for the Detection of Liquid Permittivity and Solid Displacement

Habib N. Anggradinata* and Muhamad Asvial

Department of Electrical Engineering, Universitas Indonesia, Depok 16424, Indonesia

ABSTRACT: This study proposes a dual-band microwave sensor based on a split-ring resonator (SRR) coupled with a pair of L-shaped structures. The proposed sensor has dual functionalities, including the detection of liquid permittivity and solid displacement. An ethanol-water mixture is selected as a sample to measure the permittivity of the liquid. Moreover, FR4 is chosen as the test sample to measure the displacement of the solid. As a result, the maximum frequency detection resolution (FDR) is 1.64, and the average FDR is 1.40. The maximum and average normalized sensitivity (NS) values are 0.073% and 0.06%, respectively. The maximum displacement sensitivity is 10.0 MHz/mm for f_{DS2} and 10.5 MHz/mm for f_{DS1}, while the average displacement sensitivity values are 4.98 MHz/mm and 8.02 MHz/mm for f_{DS2} and f_{DS1}, respectively. These values confirm the sensor's reliable performance and sensitivity across different measurements. In general, the proposed sensor offers several advantages: 1) it operates independently by isolating the electric fields generated by each sensor; 2) it demonstrates dual functionalities, including the detection of liquid permittivity and solid displacement; and 3) it is capable of handling both liquid and solid samples.

1. INTRODUCTION

The advancement of Internet of Things (IoT) technology is closely tied to developments in sensor technology, as sensors are critical for detecting environmental conditions [1, 2]. However, a major limitation of conventional sensors is the difficulty of integration with wireless communication systems [3, 4]. This challenge arises partly due to the significant frequency difference between traditional sensor technologies and wireless communication technologies [5–7]. To address this issue, microwave sensor technology has been introduced. Microwave sensor (MS) operates at high frequencies, enabling seamless coexistence with wireless communication systems [8, 9]. Moreover, future MS is expected to offer multifunctional capabilities rather than serving solely as standalone sensors or mono-functional one.

Several interesting studies on MS for permittivity detection have been proposed [10–17]. Ref. [18] focuses on the permittivity detection of solid materials. This study utilizes a U-resonator structure with a single port. However, it has certain limitations, such as lower sensitivity and a tendency for signal radiation due to the single-port design. Other studies, such as those by [19] and [20], have employed methods involving radio frequency identification (RFID) tags and active antenna tags, respectively. These approaches utilize reflection and frequency shift techniques. However, the proposed sensors still have complex structures and are limited to applications involving solid samples only.

Another notable study on MS was conducted by [21], which uses a dielectric resonator oscillator method with liquid samples. Changes in the liquid sample lead to shifts in the oscillator's resonance frequency, allowing for permittivity detection. While this study successfully detects the permittivity of liquids, its detection range is limited to 1.0–45.0. Further research includes [22], which employs a split-ring resonator, and [23], which utilizes a mushroom structure, both featuring planar resonator designs with liquid samples. These designs achieve a wider permittivity detection range of 1.0–80.0 through frequency shift mechanisms. Additionally, [24] proposed a study using an electric band gap resonator structure that employs phase shift as the detection mechanism. However, all of these MSs are limited to a single detection capability, focusing solely on permittivity changes.

In addition to detecting permittivity, MS can also function as displacement sensors. In study [25], a displacement sensor using a split-ring resonator (SRR) structure was proposed, where the detection mechanism is based on phase changes. However, this sensor has a limited dynamic range of only 0.6 mm. Another notable study, [26], employed a stepped impedance resonator (SIR) structure with a frequency shift detection strategy, achieving a displacement range of up to 7 mm. Similar studies include [27], which used an SRR structure, [28], which used a complementary SRR structure, and [21], which utilized a defected ground structure. Nevertheless, the primary limitation of these sensors is that they function solely as single displacement sensors [26, 27, 29–35]. In general, MS still faces several challenges: 1) multifunctional capabilities are rarely developed; 2) proposed structures often lack independence; and 3) it typically cannot handle liquid and solid samples simultaneously.

To address these issues, this study proposes novelty, as outlined below:

* Corresponding author: Habib Nurseha Anggradinata (habib.nurseha-@ui.ac.id).

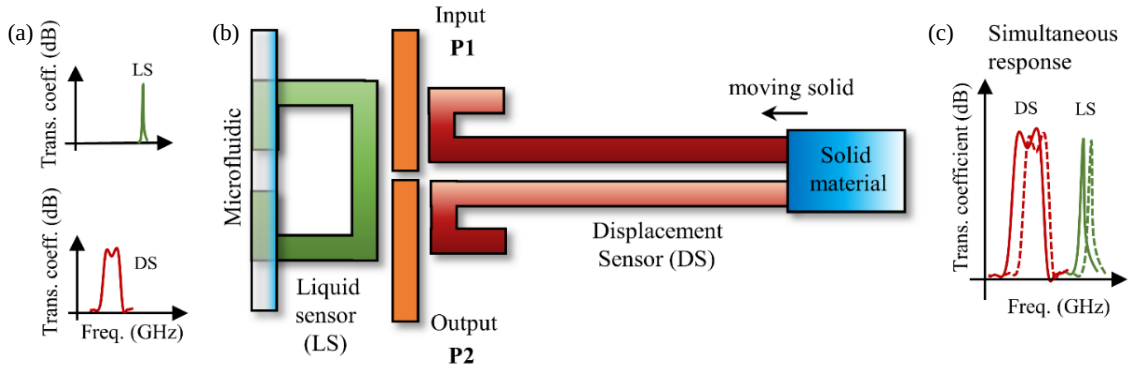

FIGURE 1. A proposed dual-band MS for detection of liquid permittivity and solid displacement, (a) transmission coefficient response for single structure, (b) integrated microwave sensor structure based on split ring resonator and coupled L-shaped resonator, and (c) simultaneous response of transmission coefficient for liquid sensor and displacement sensor.

1) This study proposes a dual-band microwave sensor based on a split-ring resonator and coupled L-shaped structures. The proposed structure operates independently by feeding-based isolation of the electric fields generated by each sensor.
2) This sensor demonstrates dual functionalities, including the detection of liquid permittivity and solid displacement.
3) Additionally, it is capable of handling both liquid and solid samples.

MS with multifunctional capabilities is highly valued because it offers several significant advantages, such as improved measurement accuracy and the ability to provide more comprehensive information about the object or material being detected. Multifunctional sensors can measure multiple parameters simultaneously, delivering richer data compared to single-function sensors. Moreover, these sensors enhance efficiency and flexibility by integrating various sensing capabilities into a single device. This approach is more efficient than using multiple separate sensors and provides greater versatility, as one sensor can serve different applications and measurement requirements. Consequently, this research addresses existing limitations by reducing system complexity and lowering the cost of component procurement. Additionally, it offers benefits in terms of cost savings, reduced space requirements, lower power consumption, and simplified maintenance.

This paper is structured as follows. Section 2 discusses the design of a microwave sensor based on a split-ring resonator and coupled L-shaped structures. It includes a proposed dual-band sensor structure and provides a complete layout structure along with a parametric iteration. Section 3 explains the simulation and optimization processes for the dual-band MS, focusing on the electric field distribution and sensing areas, followed by a detailed simulation of the MS. Section 4 presents the results and discussion of the dual-band MS. This section includes the fabrication process of the dual-band MS and evaluates its performance in detecting liquid permittivity as well as solid displacement. Finally, Section 5 concludes the paper.

2. DESIGN OF MICROWAVE SENSOR BASED ON SPLIT-RING RESONATOR AND COUPLED L-SHAPED STRUCTURES

2.1. Proposed of Dual-Band Sensor Structure

It should be noted that the proposed design enables the realization of two distinct functions: one band is dedicated to detecting permittivity, while the other band is used for displacement sensing, both operating simultaneously. By utilizing dual-band functionality, each sensing operation (permittivity and displacement) can function independently without mutual interference. This is accomplished through a design that effectively separates the operating frequencies for each sensing function. Additionally, the adoption of dual-band operation enhances sensor sensitivity, as each function can be individually optimized at its respective operating frequency. Achieving similar performance with a single-band approach would be more challenging. Integrating two sensing functions within a single dual-band device improves overall efficiency and reduces system complexity compared to deploying two separate sensors.

Several factors must be considered when designing a dual-band sensor to ensure optimal performance and accuracy. First, the sensor structure must be adapted to the type of material being detected, whether it is solid or liquid, to achieve precise and reliable measurements. Second, an isolation mechanism or blocking structure is necessary to ensure that the two frequency bands operate independently without causing interference between them. Proper isolation allows the dual-band sensor to function effectively across both bands. Lastly, the sample size plays a crucial role in the sensor design, as it influences the distribution of the electromagnetic fields, which directly impacts the sensor's sensitivity and measurement accuracy.

Figures 1(a), 1(b), and 1(c) illustrate the transmission coefficient ($|S_{21}|$) responses for three scenarios: a single structure, an integrated microwave sensor structure based on a split-ring resonator and coupled L-shaped resonator, and the simultaneous response of the transmission coefficient for both liquid and displacement sensors, respectively.

Specifically, Fig. 1(a) shows the $|S_{21}|$ response when the sensor operates independently. For the liquid sensor application,

the ($|S_{21}|$) value occurs at a higher frequency, allowing a wider range for resonance frequency shifts. In contrast, for the displacement sensor application, the ($|S_{21}|$) value is at a lower frequency with a broader bandwidth. This increased bandwidth results from the coupling of two resonators, which generates both odd and even modes. Fig. 1(b) depicts the structure of the split-ring resonator coupled with an L-shaped resonator, along with the placement of the microfluidic and displacement sensors. The resonator structure features two 50-Ohm terminations, with the split-ring resonator positioned on the left and the L-shaped resonator on the right. Additionally, a middle coupling structure was developed for facilitating the feed between the source and load. This coupled structure is crucial in blocking the electric field produced by each sensor, allowing the sensors to operate independently [36, 37]. Then, Fig. 1(c) shows the simultaneous response of the transmission coefficient for the liquid and displacement sensors, demonstrating that the sensors can operate independently.

Figure 2 shows the detailed transmission line approach for investigation for split ring resonator and coupled L-shaped resonator, respectively.

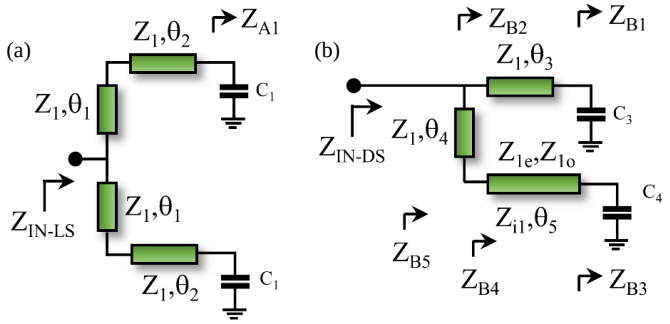

FIGURE 2. Detailed transmission line approach for investigation of (a) split ring resonator and (b) coupled L-shaped resonator.

The impedance value can be obtained as follows [36, 37]:

$$Z_{A1} = \frac{-j}{\omega C_1} \tag{1}$$

$$Z_{IN-LS} = \frac{1}{2} Z_1 \left(\frac{Z_{A1} + j \tan 2\theta_1}{1 + j Z_{A1} \tan 2\theta_1} \right) \tag{2}$$

$$Z_{B1} = \frac{-j}{\omega C_3} \tag{3}$$

$$Z_{B2} = Z_1 \left(\frac{Z_{B1} + j \tan \theta_3}{1 + j Z_{B1} \tan \theta_3} \right) \tag{4}$$

$$Z_{B3} = \frac{-j}{\omega C_4} \tag{5}$$

$$Z_{B4} = Z_{i1} \left(\frac{Z_{i1} + j \tan \theta_5}{1 + j Z_{i1} \tan \theta_5} \right) \tag{6}$$

$$Z_{B5} = Z_1 \left(\frac{Z_{B4} + j \tan \theta_4}{1 + j Z_{B4} \tan \theta_4} \right) \tag{7}$$

$$Z_{IN-DS} = \frac{Z_{B2} Z_{B5}}{Z_{B2} + Z_{B5}} \tag{8}$$

It should be noted that some of the advantages of using an SRR as a resonator include the separation of the electric field from the magnetic field. Consequently, the electric field can be optimized to detect changes in the permittivity of a sample. Moreover, SRRs can be easily integrated with other microstrip components or circuits, enabling the development of complex wireless systems. Then, the next step is focused on parametric study of sensor dimension. This is important to obtaining initial frequency response of the proposed sensor structure.

2.2. Complete Layout Structure and Parametric Iteration

Figure 3 shows a complete layout of split ring and coupled L-shaped resonator structures including the dimension. It can be seen that the sensor has a dual-port configuration. Then, it is connected to 50 Ohm termination. Then, the proposed sensor was simulated on a Rogers RT/Duroid 5880 substrate with a permittivity (ε_r) of 2.2, a thickness (h) of 1.6 mm, and tan d of 0.0009. The advantages of using Rogers RT/Duroid 5880 material can be seen in its low loss tangent value of 0.0009. This results in low sensor attenuation.

Moreover, Figs. 4(a), 4(b), 4(c), and 4(d) show the transmission coefficient values with different lengths of L_1, transmission coefficient ($|S_{21}|$) values with different lengths of W_4, transmission coefficient values with different gaps of S_3, and transmission coefficient values with different gaps of S_4, respectively.

In detail, Fig. 4(a) shows that the length of L_1 significantly influences the upper frequency, or the frequency of the ring resonator. Therefore, adjusting the value of L_1 allows for optimization to achieve the desired frequency for the liquid sensor. Fig. 4(b) presents the results of the dimensional iteration for the length of W_4. The simulation results indicate that W_4 significantly affects the resonance position of the displacement sensor, with longer W_4 dimensions leading to lower frequency values. Fig. 4(c) shows the simulation and dimensional iteration results for s_3, the gap between the liquid sensor and the feeder. As the gap s_3 increases, the ($|S_{21}|$) value decreases. Additionally, it is observed that the resonance frequency of the displacement sensor becomes more stable. Fig. 4(d) illustrates the simulation results of the coupling between the displacement sensor and the feeder channel. These results demonstrate that increasing the gap s_4 results in a lower ($|S_{21}|$) value. The next stage involves simulation and optimization of the sensing region.

3. SIMULATION AND OPTIMIZATION OF DUAL-BAND MICROWAVE SENSORS

3.1. Electric Field Distribution and Sensing Areas

Figures 5(a), 5(b), and 5(c) illustrate the electric field distribution for sensing region of liquid sensor at $f_{LS} = 2.234$ GHz, sensing region of displacement sensor at $f_{DS2} = 1.634$ GHz, and (b) sensing region of displacement sensor at $f_{DS1} = 1.819$ GHz, respectively. The electric field distribution has same scale from 0 kV/m to 30 kV/m. Then, Fig. 5(a) shows that the electric field at the split ring resonator occurs at the gap region. At frequencies $W_A = 1.634$ GHz and $l_A = 1.819$ GHz,

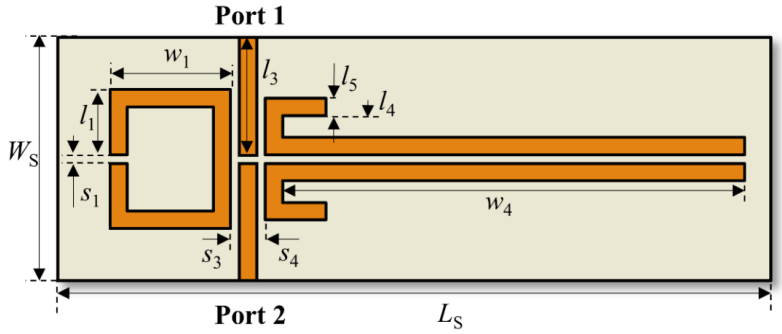

FIGURE 3. A complete layout of split ring and coupled L-shaped resonator structures. Here, the dimension values are $w_1 = 10.0\,\text{mm}$, $w_2 = 2.0\,\text{mm}$, $w_3 = 5.0\,\text{mm}$, $w_4 = 53.5\,\text{mm}$, $l_1 = 7.5\,\text{mm}$, $l_2 = 12.0\,\text{mm}$, $l_3 = 11.5\,\text{mm}$, $l_4 = 6.5\,\text{mm}$, $l_5 = 2.0\,\text{mm}$, $l_5 = 6.0\,\text{mm}$, $s_1 = 1.0\,\text{mm}$, $s_2 = 1.0\,\text{mm}$, $s_2 = 1.0\,\text{mm}$, $s_4 = 1.0\,\text{mm}$, $W_S = 24\,\text{mm}$, and $L_S = 100\,\text{mm}$.

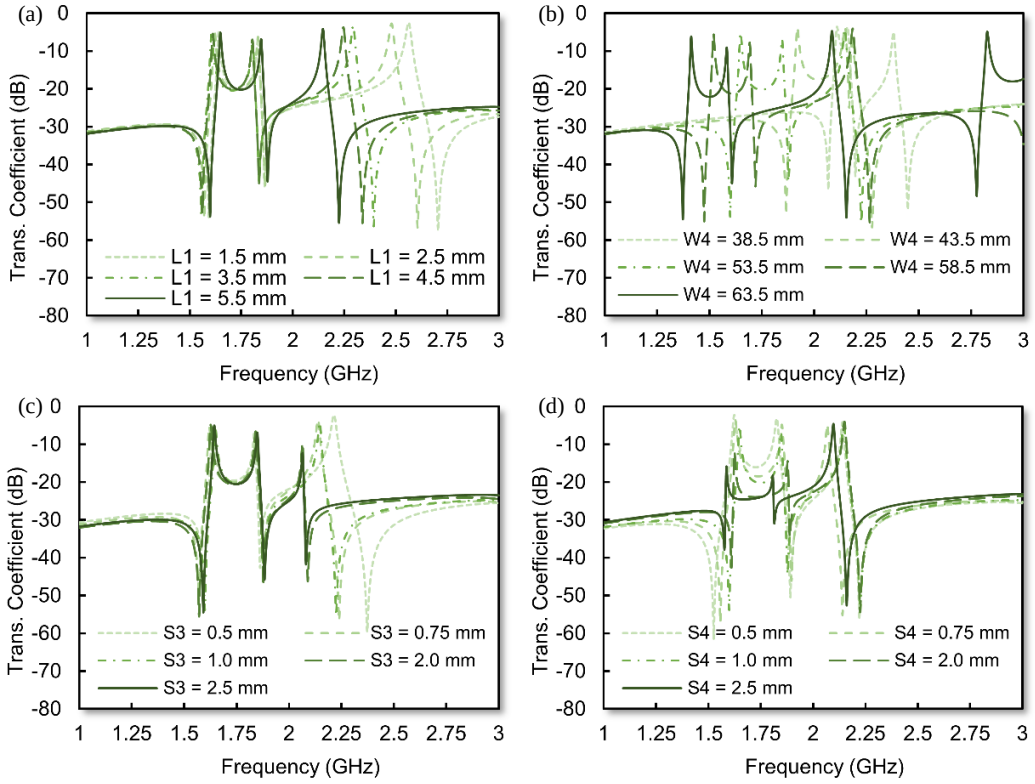

FIGURE 4. (a) Transmission coefficient values with different lengths of L_1, (b) transmission coefficient values with different lengths of W_4, (c) transmission coefficient values with different gaps of S_3, and (d) transmission coefficient values with different gaps of S_4.

the electric field reaches its maximum value in the sensing region, which functions as a displacement sensor. Additionally, a low electric field coupling is observed between the liquid sensor and the displacement sensor, indicating minimal interference between the two sensors. Simulation of the electric field distribution reveals that the electric field is focused on the corresponding sensing area for each sensor. The electric field coupling between the two sensors is also low, so no interference occurs. This confirms the good operation separation between the liquid sensor and the displacement sensor. The simulation was conducted using a CST simulator. The CST simulation operates based on the Finite Integration Technique (FIT).

Figures 6(a) and 6(b) show the final layout of proposed split ring and coupled L-shaped resonator structure, and perpendicular view of proposed split ring and coupled L-shaped resonator structure for liquid permittivity and solid displacement detection, respectively. In detail, Fig. 6(a) shows that the microfluidic channel has dimension of $r_{in} = 1\,\text{mm}$, $r_{out} = 1.5\,\text{mm}$. For solid displacement detection, the FR4 substrate with a permittivity (ε_r) of 4.3, a thickness (h) of 1.6 mm, and tan d of 0.0265 was used. Moreover, the solid sample dimension of $w_A = 10\,\text{mm}$ and $l_A = 20\,\text{mm}$. Then, the proposed sensor structure has a full ground-plane structure, as shown in Fig. 6(b).

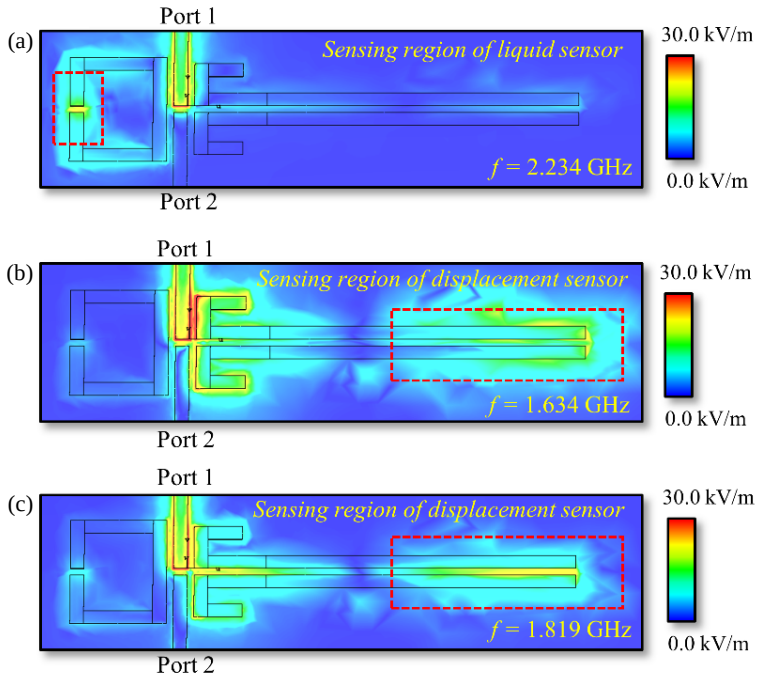

FIGURE 5. Electric field distribution for (a) sensing region of liquid sensor at $f = 2.234$ GHz, (b) sensing region of displacement sensor at $f = 1.634$ GHz, and (b) sensing region of displacement sensor at $f = 1.819$ GHz.

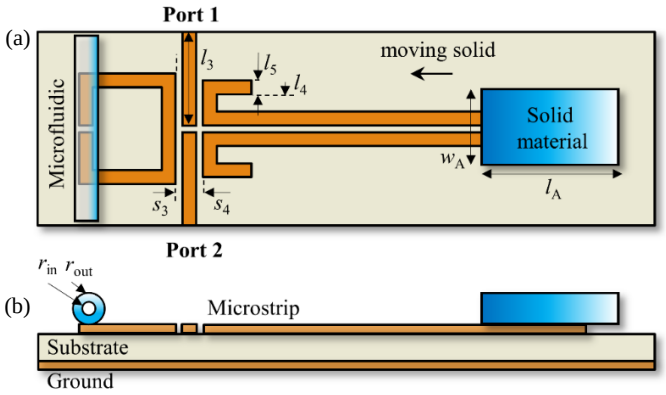

FIGURE 6. (a) Final layout of proposed split ring and coupled L-shaped resonator structure, and (b) perpendicular view of proposed split ring and coupled L-shaped resonator structure for liquid permittivity and solid displacement detection where $r_{in} = 1$ mm, $r_{out} = 1.5$ mm, and solid sample dimension of $w_A = 10$ mm and $l_A = 20$ mm.

3.2. Simulation of Microwave Sensors

Figures 7(a), 7(b), and 7(c) show the transmission coefficient with different values of relative permittivity, transmission coefficient with different values of loss tangent, and transmission coefficient with different values of solid displacements, respectively. The simulation shows that the peak frequency position of the liquid sensor shifts as the permittivity value varies from 1.0 to 80.0. As the permittivity increases, the liquid sensor's peak shifts further to the left, as shown in Fig. 7(a). Meanwhile, an increase in the $\tan\delta$ results in a decrease in the magnitude of the transmission coefficient. Additionally, the response of the displacement sensor remains stable, demonstrating that the sensors can operate independently, as illustrated in Fig. 7(b). Then, Fig. 7(c) shows the independent response of the sensors. Specifically, when the solid material is shifted by a distance of 1.0 to 10.0 mm, only the transmission coefficient of the displacement sensor shifts, while the liquid sensor does not exhibit any significant shift.

4. RESULT AND DISCUSSION OF DUAL-BAND MICROWAVE SENSORS

4.1. Fabrication of Dual-Band Microwave Sensor

Figures 8(a), 8(b), 8(c), and 8(d) illustrate the measurement setup of integrated and independent dual-band MS for the detection of liquid permittivity and solid displacement, liquid permittivity sensor, and displacement solid sensor, respectively.

Figure 8(a) shows the sensor connected to a vector network analyzer (VNA) device with a 50-Ohm SMA termination. The figure also illustrates multiple peaks in the transmission coefficient, corresponding to the liquid sensor (LS) and displacement sensor (DS) applications. For the displacement sensor, two peaks are observed in the transmission coefficient. At higher frequencies, harmonic responses are also visible; however, these harmonics are not utilized in this study, as they introduce additional complexity and may produce other complex modes. The liquid sample used is ethanol, with concentrations ranging from 0% to 100% in increments of 10%. Fig. 8(b) shows the microfluidic setup, including the inlet and outlet for introducing the liquid sample. Fig. 8(c) illustrates the displacement sensor with a solid material sample. To aid in precise measurements during the investigation, mm-grid paper is used as a step reference value. Fig. 8(d) shows the size of MS for detection of liquid permittivity and solid displacement.

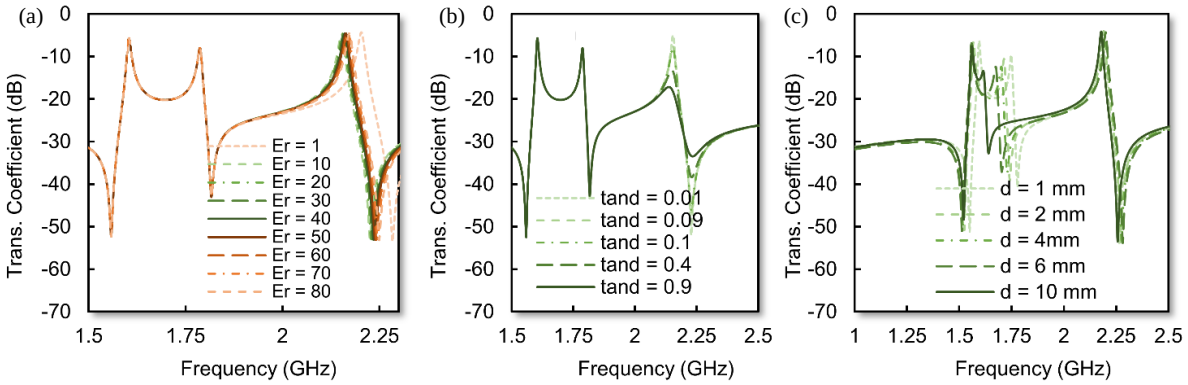

FIGURE 7. (a) Transmission coefficient with different values of relative permittivity, (b) transmission coefficient with different values of loss tangent, and (c) transmission coefficient with different values of solid displacements.

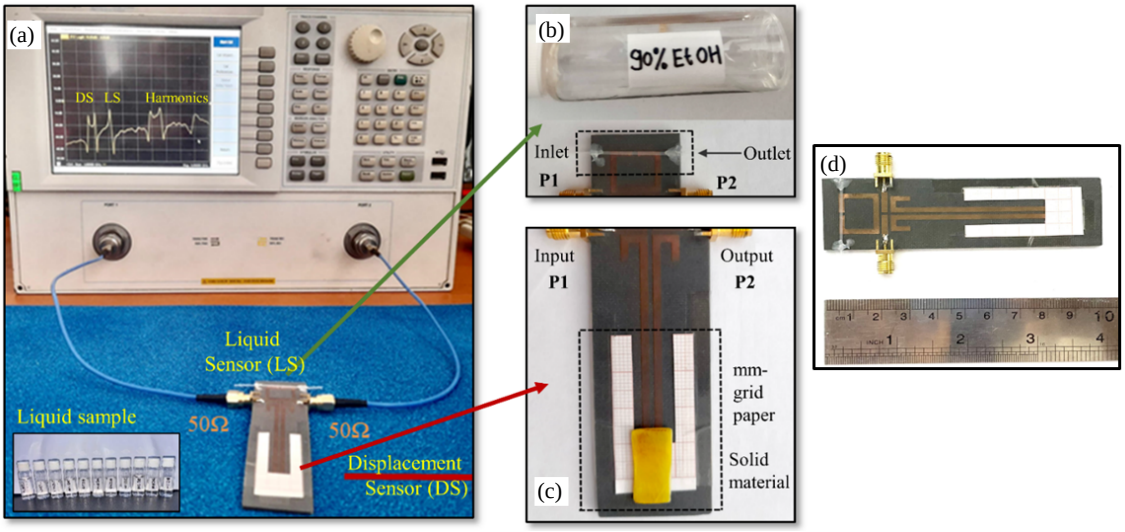

FIGURE 8. (a) Measurement setup of integrated and independent dual-band MS for detection of liquid permittivity and solid displacement, (b) liquid permittivity sensor, (c) displacement solid sensor, and (d) size MS.

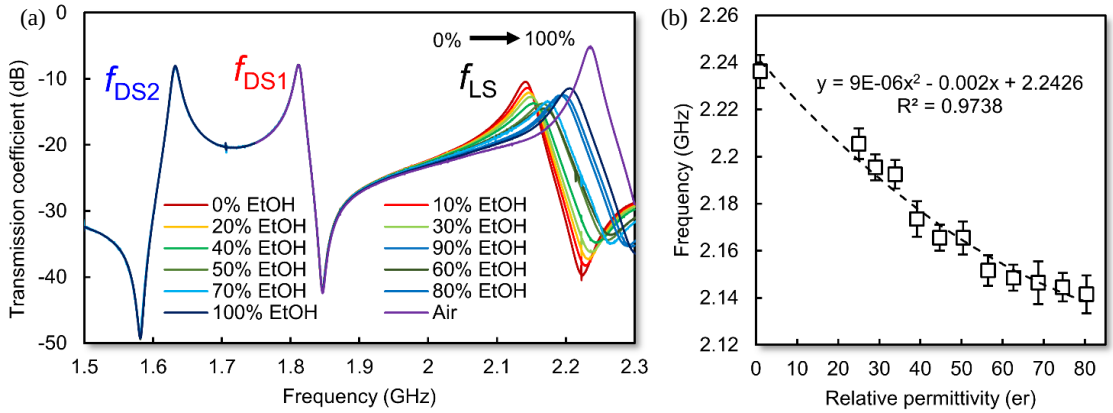

FIGURE 9. (a) Transmission coefficient response with different ethanol concentrations, and (b) the frequency value at maximum transmission coefficient with different relative permittivities.

4.2. Evaluation of Liquid Permittivity Detection

Figures 9(a) and 9(b) show the transmission coefficient response with different ethanol concentrations, and the frequency value at maximum transmission coefficient with different relative permittivities, respectively. Moreover, changes in the relative permittivity of the liquid due to variations in ethanol con-

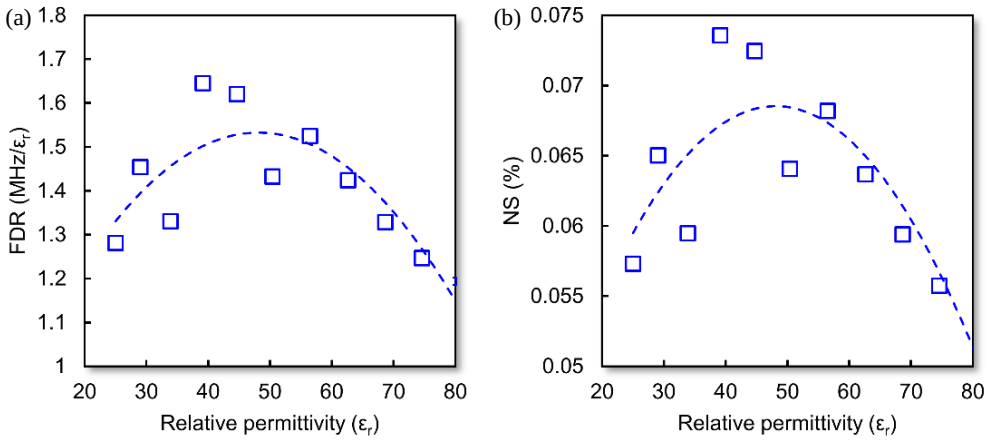

FIGURE 10. (a) FDR value with different relative permittivities, and (b) NS value with different relative permittivities.

centration cause a shift in the resonant frequency of the liquid sensor. The higher the ethanol concentration is, the greater the shift is in resonance frequency of the liquid sensor towards higher. This allows the sensor to be used in ethanol concentration detection applications accurately. The correlation values can be evaluated using R^2. The closer the value is to one, the higher the correlation is. Fig. 9(b) shows an R^2 value of 0.9738 between the frequency position and permittivity value. The margin of error can be calculated using 1-R^2. Therefore, the margin of error is approximately 1–3%. Then, Figs. 10(a) and 10(b) show FDR values with different relative permittivities, and NS values with different relative permittivities.

Figure 9(a) clearly demonstrates that the peak transmission coefficient frequency (f_{LS}) shifts with varying ethanol concentrations. At 0% ethanol (pure water), the peak f_{LS} occurs at 2.141 GHz with a magnitude of -10.52 dB. In unloaded conditions (without a sample), the f_{LS} peak is located at 2.236 GHz with a magnitude of -5.173 dB. Additionally, Fig. 9(a) shows that the peak values for the displacement sensor remain stable. The upper frequency peak (f_{DS1}) occurs at 1.631 GHz with a magnitude of -8.47 dB, while the lower frequency peak (f_{DS2}) is at 1.811 GHz with a magnitude of -8.01 dB. These measurements confirm that the liquid sensor operates independently.

To ensure the stability of the sensor, measurements were conducted five times under controlled environmental conditions, with a room temperature of 29°C and humidity at 60%. For evaluation purposes, the ethanol concentration values were interpreted as permittivity values. Details regarding the relationship between ethanol concentration and its corresponding permittivity values can be found in [38]. Fig. 9(b) illustrates a strong correlation between changes in permittivity and frequency shifts. The resulting regression equation yields an R^2 value of 0.9738, indicating a very high correlation between concentration changes and frequency shifts. To evaluate the performance of the liquid sensor, we utilize FDR and NS. The equation for calculating FDR is as follows [39, 40]

$$\mathrm{FDR} = \left| \frac{f - f_0}{\Delta \varepsilon_r} \right| \tag{9}$$

Then, the normalized sensitivity value is defined as follows [41]:

$$NS\,(\%) = \left| \frac{f - f_0}{f_0\,(\varepsilon_r - 1)} \right| \times 100 \tag{10}$$

where $NS(\%)$ is the sensitivity of permittivity sensor, and f_0 stands for the frequency when air is used as the sample. Fig. 10(a) and 10(b) show FDR value with different relative permittivities, and NS value with different relative permittivities, respectively. The maximum FDR value is 1.64. Then, the average FDR is 1.40. Moreover, the maximum and average of NS are 0.073% and 0.06%, respectively.

4.3. Evaluation of Solid Displacement Detection

Figure 11 shows the transmission coefficient response with different solid displacement distances. It can be observed that f_{DS1} and f_{DS2} shift, with the magnitude of the shift decreasing as the frequency change becomes smaller. Meanwhile, f_{LS} remains stable at a frequency of 2.243 GHz with a magnitude of -4.71 dB. This indicates that the sensors operate independently.

Figures 12(a) and 12(b) show the frequency value at maximum transmission coefficient with different solid displacements and sensitivity value with different solid displacements, respectively. It can be seen that the f_{DS1} and f_{DS2} frequencies exhibit values of $R^2 = 0.997$ and $R^2 = 0.990$, respectively, indicating a strong correlation between displacement distance and frequency shift. This high correlation demonstrates the sensor's effectiveness in detecting displacement changes. The maximum displacement sensitivity is 10.0 MHz/mm for f_{DS2} and 10.5 MHz/mm for f_{DS1}, while the average displacement sensitivity values are 4.98 MHz/mm and 8.02 MHz/mm for f_{DS2} and f_{DS1}, respectively. These values confirm the sensor's reliable performance and sensitivity across different measurements. The margin of error can be calculated using 1-R^2. Therefore, the margin of error is approximately 1–3%.

The advantages of the design for displacement detection is that the displacement sensor has a high sensitivity that can detect changes in position or solid displacement. The change in

TABLE 1. Comparison with previous result.

Ref.	Method and year	Num. Freq.	Sensing mechanism	Range of εr	Liquid sensor		Displacement sensor		Sample		Size (mm^2)	Dual functional
					FDR (MHz/εr)	NS (%)	Dynamics range (mm)	Sensitivity (MHz/mm)	Liquid	Solid		
[19]	RFID Antenna (2018)	1	Reflection	1.0 – 12.85	2.60	0.100	-	-	-	Rogers	1018.6	-
[20]	Active tag antenna (2017)	2	Freq. shift	1.0 – 10.2	2.30	0.340	-	-	-	Rogers	>2400	-
[21]	Dielectric resonator (2012)	1	Freq. shift	1.0 – 45.0	NA	0.002	-	-	2-Butyl Alcohol, Xylene, ect	-	702	-
[22]	Split-ring resonator (2014)	1	Freq. shift	1.0 – 80.0	1.50	0.003	-	-	Hexane, Ethanol, Methanol	-	1296	-
[23]	Mushroom Structure (2019)	1	Freq. shift	1.0 – 80.0	3.00	0.040	-	-	Isopropyl Alcohol, Ethanol, Methanol, etc	-	>2400	-
[24]	Electric band gap (2017)	1	Phase. shift	1.0 – 80.0	NA	0.008	-	-	Toluene, Methanol	-	1796.8	-
[3]	SRR, pulse-resonator, and two U – Resonators (2024)	1	Freq. shift	1.0 – 78	0.04	0.64	-	-	Ethanol, Methannol, Glucose, Deionized water	-	700	-
[42]	Substrate Integrated Waveguide (2022)	1	Freq. shift	56.3 – 63	7.67	0.681	-	-	Blood Glucose	-	756	-
[18]	Dual U – Resonators (2022)	2	Freq. shift	1.0 – 4.3	NA	0.76	-	-	-	Air, RO5880, RO4003C, FR4	>2400	-
[43]	Multifrequency coupled-resonator (2021)	1	Freq. shift	2.36 – 78.80	NA	0.17 - 0.30	-	-	DI Water, Acetonitrile, Methyl hydrate, Acetone, ect	-	764.4	-
[44]	T – Resonators (2024)	1	Freq. shift	1.0 – 6.15	0.016	5.13	-	-	-	Air, RO5880, RO4003C, FR4, RO3006	>2400	-
[45]	Complementary SRR (2024)	1	Freq. shift	1.0 – 80.0	149.2	0.149	-	-	Ethanol	-	1200	-
[37]	Asymmetric Ring Resonator (2023)	1	Freq. shift	1.0 – 80.0	NA	0.016			Ethanol	-	>2400	-
[46]	Defected ground structure (2016)	1	Freq. shift	-	-	-	3.0	72.0	-	NA	NA	-
[25]	SRR (2012)	1	Ref. mode	-	-	-	0.6	NA	-	Rogers	133.33	-
[26]	Step impedance (2022)	1	Freq. shift	-	-	-	7.0	52.0	-	Rogers RO3006	NA	-
[27]	SRR (2014)	1	Freq. shift	-	-	-	3.0	41.0	-	Rogers RO4003	>2400	-
[28]	Complementary SRR (2011)	1	Freq. shift	-	-	-	7.0	43.0	-	NA	616	-
This work	SRR and Coupled L-Resonators	2	Freq. shift	1.0 – 80.0	1.64	0.073	12.0	10.5	Ethanol	FR4	2400	yes

FDR = frequency detection range, NA = not available information, NS = Normalized sensitivity.

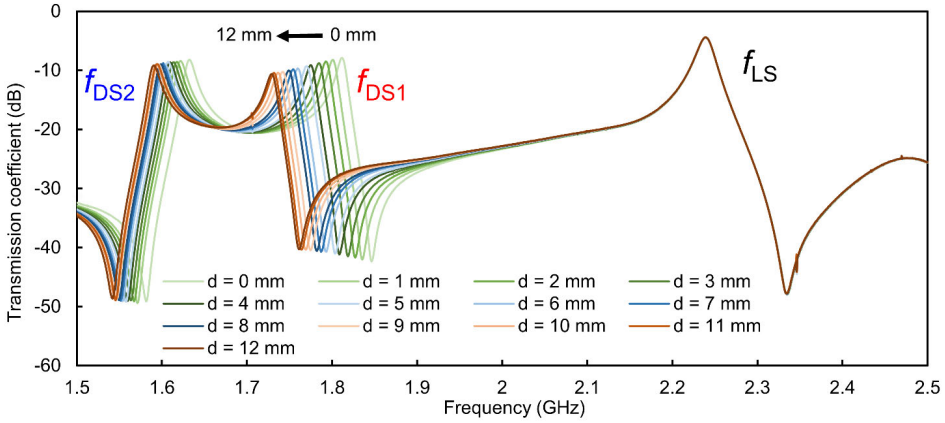

FIGURE 11. Transmission coefficient response with different solid displacements.

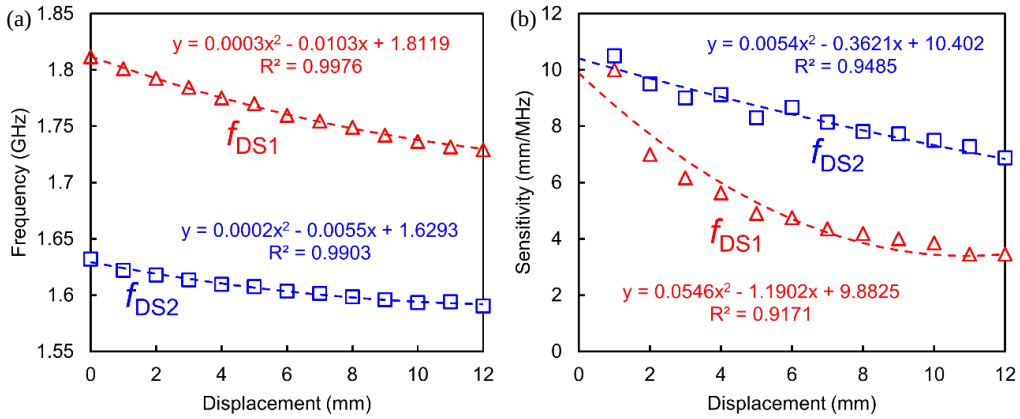

FIGURE 12. (a) The frequency value at maximum transmission coefficient with different solid displacements, and (b) sensitivity value with different solid displacements.

solid displacement will cause a shift in the resonant frequency of the sensor (f_{DS1} and f_{DS2}) which can be measured well. The response of the displacement sensor is only affected by changes in solid displacement, without being affected by the response of the liquid sensor. This enables independent measurement of solid displacement without interference from liquid measurement. The limitations of the design for displacement detection are that the limited measurement range may limit the application of the sensor, and the integration of the displacement sensor and liquid sensor in a single device may add to the complexity of the design and fabrication. This can increase the cost and challenges in implementation.

Table 1 highlights the position and advantages of this research. In previous studies, many MSs have been proposed to detect the permittivity function with liquid and solid sample characteristics. There are other studies of MS as a function of displacement with solid characteristics as a sample material that have been researched. This study has successfully designed a dual-band microwave sensor using an SRR and a coupled L-shaped structure. On the sensor performance and results obtained, the proposed sensor can work dual bands with two functions, first band for permittivity detection and second band for displacement sensor, both of which can work simultaneously. While the NS value for the liquid sensor is relatively high, the displacement sensitivity is slightly lower. However, this study demonstrates the sensor's ability to evaluate displacement over a wider dynamic range with dual functional capabilities. However, it should be noted that the main disadvantage of MS lies in its nonlinear nature, which is evident in the responses of both the liquid sensor and displacement sensor. This nonlinearity arises from the fundamental capacitance equation, which is inversely proportional to distance. As a direction for future research, the investigation of nonlinear properties and the use of modified SRR structures could be explored to achieve higher sensitivity. Overall, this research has potential for future development in IoT applications, particularly for environmental monitoring involving liquid and solid materials.

5. CONCLUSION

This study has successfully designed a dual-band microwave sensor using a split-ring resonator and coupled L-shaped structures for detecting liquid permittivity and solid displacement. The sensor is fabricated on a Rogers RT/Duroid 5880 substrate with a permittivity of 2.2, a thickness of 1.6 mm, and a loss tangent of 0.0009. An ethanol-water mixture is selected as a sam-

ple to measure the permittivity of the liquid. Moreover, FR4 is chosen as the test sample to measure the displacement of the solid. As a result, the maximum FDR is 1.64, and the average FDR is 1.40. The maximum and average NS values are 0.073% and 0.06%, respectively. The maximum displacement sensitivity is 10.0 MHz/mm for f_{DS2} and 10.5 MHz/mm for f_{DS1}, while the average displacement sensitivity values are 4.98 MHz/mm and 8.02 MHz/mm for f_{DS2} and f_{DS1}, respectively. These values confirm the sensor's reliable performance and sensitivity across different measurements. In the future, a potential application identified for this sensor in IoT technology is in the industrial sector, where it could serve as a solution for direct measurement and detection in storage system tanks. Permittivity sensors can operate as quality monitors for the contents of storage tanks through pipes or delivery hoses, while displacement sensors can function as quantity monitors for the tank contents. Additionally, these sensors can be applied to monitor and measure both the quality and quantity of water in dams, rivers, and drainage systems within the environmental sector.

REFERENCES

[1] Abdolrazzaghi, M. and M. Daneshmand, "Exploiting sensitivity enhancement in micro-wave planar sensors using intermodulation products with phase noise analysis," *IEEE Transactions on Circuits and Systems I: Regular Papers*, Vol. 67, No. 12, 4382–4395, 2020.

[2] Zhu, L., M. Farhat, Y.-C. Chen, K. N. Salama, and P.-Y. Chen, "A compact, passive frequency-hopping harmonic sensor based on a microfluidic reconfigurable dual-band antenna," *IEEE Sensors Journal*, Vol. 20, No. 21, 12 495–12 503, 2020.

[3] Alam, S., I. Surjati, L. Sari, Y. K. Ningsih, M. Y. Fathanah, Y. K. Gultom, G. Daffin, T. Firmansyah, and Z. Zakaria, "UHF-band solid sensor based on tweaking electric field coupled resonator for material characterization," *Progress In Electromagnetics Research M*, Vol. 126, 11–18, 2024.

[4] Bait-Suwailam, M. M., "Numerical assessment of red palm weevil detection mechanism in palm trees using CSRR microwave sensors," *Progress In Electromagnetics Research Letters*, Vol. 100, 63–71, 2021.

[5] Kobayashi, Y., T. Tsuchiya, M. Okazaki, Y. Asao, K. Hashimoto, and S. Shikata, "High-frequency surface acoustic wave resonator with ScAlN/hetero-epitaxial diamond," *Diamond and Related Materials*, Vol. 111, 108190, 2021.

[6] Go, D. B., M. Z. Atashbar, Z. Ramshani, and H.-C. Chang, "Surface acoustic wave devices for chemical sensing and microfluidics: A review and perspective," *Analytical Methods*, Vol. 9, No. 28, 4112–4134, 2017.

[7] Shilton, R. J., M. Travagliati, F. Beltram, and M. Cecchini, "Nanoliter-droplet acoustic streaming via ultra high frequency surface acoustic waves," *Advanced Materials*, Vol. 26, No. 29, 4941–4946, 2014.

[8] Ebrahimi, A., J. Scott, and K. Ghorbani, "Dual-mode resonator for simultaneous permittivity and thickness measurement of dielectrics," *IEEE Sensors Journal*, Vol. 20, No. 1, 185–192, 2020.

[9] Albishi, A. M., M. K. E. Badawe, V. Nayyeri, and O. M. Ramahi, "Enhancing the sensitivity of dielectric sensors with multiple coupled complementary split-ring resonators," *IEEE Transactions on Microwave Theory and Techniques*, Vol. 68, No. 10, 4340–4347, 2020.

[10] Tseng, C.-H. and C.-Y. Yang, "Novel microwave frequency-locked-loop-based sensor for complex permittivity measurement of liquid solutions," *IEEE Transactions on Microwave Theory and Techniques*, Vol. 70, No. 10, 4556–4565, 2022.

[11] Kulkarni, S. and M. S. Joshi, "Design and analysis of shielded vertically stacked ring resonator as complex permittivity sensor for petroleum oils," *IEEE Transactions on Microwave Theory and Techniques*, Vol. 63, No. 8, 2411–2417, 2015.

[12] Kiani, S., P. Rezaei, M. Navaei, and M. S. Abrishamian, "Microwave sensor for detection of solid material permittivity in single/multilayer samples with high quality factor," *IEEE Sensors Journal*, Vol. 18, No. 24, 9971–9977, 2018.

[13] Su, L., J. Muñoz-Enano, P. Vélez, P. Casacuberta, M. Gil, and F. Martin, "Phase-variation microwave sensor for permittivity measurements based on a high-impedance half-wavelength transmission line," *IEEE Sensors Journal*, Vol. 21, No. 9, 10 647–10 656, 2021.

[14] Sun, H., R. Li, G. Y. Tian, T. Tang, G. Du, and B. Wang, "Determination of complex permittivity of thin dielectric samples based on high-Q microstrip resonance sensor," *Sensors and Actuators A: Physical*, Vol. 296, 31–37, 2019.

[15] Yeo, J. and J.-I. Lee, "Slot-loaded microstrip patch sensor antenna for high-sensitivity permittivity characterization," *Electronics*, Vol. 8, No. 5, 502, 2019.

[16] Li, Y., N. Bowler, and D. B. Johnson, "A resonant microwave patch sensor for detection of layer thickness or permittivity variations in multilayered dielectric structures," *IEEE Sensors Journal*, Vol. 11, No. 1, 5–15, 2011.

[17] Coromina, J., J. Muñoz-Enano, P. Vélez, A. Ebrahimi, J. Scott, K. Ghorbani, and F. Martín, "Capacitively-loaded slow-wave transmission lines for sensitivity improvement in phase-variation permittivity sensors," in *2020 50th European Microwave Conference (EuMC)*, 491–494, Utrecht, Netherlands, Jan. 2021.

[18] Alam, S., Z. Zakaria, I. Surjati, N. A. Shairi, M. Alaydrus, and T. Firmansyah, "Dual-band independent permittivity sensor using single-port with a pair of U-shaped structures for solid material detection," *IEEE Sensors Journal*, Vol. 22, No. 16, 16 111–16 119, 2022.

[19] Saghlatoon, H., R. Mirzavand, M. M. Honari, and P. Mousavi, "Sensor antenna transmitter system for material detection in wireless-sensor-node applications," *IEEE Sensors Journal*, Vol. 18, No. 21, 8812–8819, 2018.

[20] Adhikary, M., A. Biswas, and M. J. Akhtar, "Active integrated antenna based permittivity sensing tag," *IEEE Sensors Letters*, Vol. 1, No. 6, 1–4, 2017.

[21] Sekar, V., W. J. Torke, S. Palermo, and K. Entesari, "A self-sustained microwave system for dielectric-constant measurement of lossy organic liquids," *IEEE Transactions on Microwave Theory and Techniques*, Vol. 60, No. 5, 1444–1455, 2012.

[22] Abduljabar, A. A., D. J. Rowe, A. Porch, and D. A. Barrow, "Novel microwave microfluidic sensor using a microstrip split-ring resonator," *IEEE Transactions on Microwave Theory and Techniques*, Vol. 62, No. 3, 679–688, 2014.

[23] Gargari, A. M., M. H. Zarifi, and L. Markley, "Passive matched mushroom structure for a high sensitivity low profile antenna-based material detection system," *IEEE Sensors Journal*, Vol. 19, No. 15, 6154–6162, 2019.

[24] Radonić, V., S. Birgermajer, and G. Kitić, "Microfluidic EBG sensor based on phase-shift method realized using 3D printing technology," *Sensors*, Vol. 17, No. 4, 892, 2017.

[25] Martín, F., M. Durán-Sindreu, and F. Martín, "Alignment and position sensors based on split ring resonators," *Sensors*, Vol. 12, No. 9, 11 790–11 797, 2012.

[26] Mehrjoo, Z., A. Ebrahimi, and K. Ghorbani, "Microwave resonance-based reflective mode displacement sensor with wide dynamic range," *IEEE Transactions on Instrumentation and Measurement*, Vol. 71, 1–9, 2021.

[27] Horestani, A. K., J. Naqui, Z. Shaterian, D. Abbott, C. Fumeaux, and F. Martín, "Two-dimensional alignment and displacement sensor based on movable broadside-coupled split ring resonators," *Sensors and Actuators A: Physical*, Vol. 210, 18–24, 2014.

[28] Mandel, C., B. Kubina, M. Schüßler, and R. Jakoby, "Passive chipless wireless sensor for two-dimensional displacement measurement," in *2011 41st European Microwave Conference*, 79–82, Manchester, UK, Oct. 2011.

[29] Naqui, J. and F. Martín, "Transmission lines loaded with bisymmetric resonators and their application to angular displacement and velocity sensors," *IEEE Transactions on Microwave Theory and Techniques*, Vol. 61, No. 12, 4700–4713, 2013.

[30] Teng, C., C. H. Chio, K. W. Tam, and P. Y. Lau, "An angular displacement microwave sensor with 360° dynamic range using multi-mode resonator," *IEEE Sensors Journal*, Vol. 21, No. 3, 2899–2907, 2021.

[31] Chio, C. H., R. Gómez-García, L. Yang, K. W. Tam, W.-W. Choi, and S. K. Ho, "An angular displacement sensor based on microwave transversal signal interference principle," *IEEE Sensors Journal*, Vol. 20, No. 19, 11 237–11 246, 2020.

[32] Zhu, H.-X., P. Cheong, K.-W. Tam, S.-K. Ho, and W.-W. Choi, "An angular displacement sensor based on microstrip wideband impedance transformer with quasi-Chebyshev frequency response," *IEEE Sensors Journal*, Vol. 20, No. 8, 4200–4206, 2020.

[33] Naqui, J. and F. Martín, "Angular displacement and velocity sensors based on electric-LC (ELC) loaded microstrip lines," *IEEE Sensors Journal*, Vol. 14, No. 4, 939–940, 2014.

[34] Chio, C.-H., K.-W. Tam, and R. Gómez-García, "Filtering angular displacement sensor based on transversal section with parallel-coupled-line path and U-shaped coupled slotline," *IEEE Sensors Journal*, Vol. 22, No. 2, 1218–1226, 2022.

[35] Chio, C.-H., R. Gómez-García, L. Yang, K.-W. Tam, W.-W. Choi, and S.-K. Ho, "An angular-displacement microwave sensor using an unequal-length-bi-path transversal filtering section," *IEEE Sensors Journal*, Vol. 20, No. 2, 715–722, 2020.

[36] Pozar, D. M., *Microwave Engineering*, 4th ed., 752, John Wiley & Sons, 2011.

[37] Verma, A. K., *Introduction to Modern Planar Transmission Lines: Physical, Analytical, and Circuit Models Approach*, John Wiley & Sons, 2021.

[38] Ebrahimi, A., J. Scott, and K. Ghorbani, "Ultrahigh-sensitivity microwave sensor for microfluidic complex permittivity measurement," *IEEE Transactions on Microwave Theory and Techniques*, Vol. 67, No. 10, 4269–4277, 2019.

[39] Firmansyah, T., S. Praptodiyono, I. Muttakin, K. Paramayudha, S. Alam, T. Handoyo, D. Rusdiyanto, M. Alaydrus, H. N. Anggradinata, T. Abuzairi, G. Wibisono, and J. Kondoh, "Multifunctional glass microfluidic microwave sensor attenuator for detection of permittivity and conductivity with device protection," *IEEE Sensors Journal*, Vol. 24, No. 4, 4574–4585, 2024.

[40] Firmansyah, T., S. Praptodiyono, I. Muttakin, M. Wildan, D. A. Cahyasiwi, Y. Rahayu, H. Ludiyati, K. Paramayudha, Y. Wahyu, S. Alam, M. Alaydrus, and J. Kondoh, "Integrated and independent solid microwave sensor with dual-band bandpass filter through unified mux-demux structure," *IEEE Sensors Journal*, Vol. 24, No. 12, 19 253–19 261, 2024.

[41] Abdolrazzaghi, M., M. Daneshmand, and A. K. Iyer, "Strongly enhanced sensitivity in planar microwave sensors based on metamaterial coupling," *IEEE Transactions on Microwave Theory and Techniques*, Vol. 66, No. 4, 1843–1855, 2018.

[42] Kiani, S. and P. Rezaei, "Microwave substrate integrated waveguide resonator sensor for non-invasive monitoring of blood glucose concentration: Low cost and painless tool for diabetics," *Measurement*, Vol. 219, 113232, 2023.

[43] Sepulveda, L. V. H., J. L. O. Cervantes, and C. E. Saavedra, "Multifrequency coupled-resonator sensor for dielectric characterization of liquids," *IEEE Transactions on Instrumentation and Measurement*, Vol. 70, 1–7, 2021.

[44] Alam, S., Z. Zakaria, I. Surjati, N. A. Shairi, M. Alaydrus, T. Firmansyah, Y. K. Ningsih, and L. Sari, "Collaboratively far-field and near-field regions for dual-modalities microwave permittivity sensor using T-shaped resonator embedded with IDC," *IEEE Sensors Letters*, Vol. 8, No. 7, 1–4, 2024.

[45] Han, X., K. Liu, and S. Zhang, "High-sensitivity dual-band microfluidic microwave sensor for liquid dielectric characterization," *IEEE Sensors Journal*, Vol. 24, No. 22, 36 689–36 697, 2024.

[46] Rezaee, M. and M. Joodaki, "Two-dimensional displacement sensor based on CPW line loaded by defected ground structure with two separated transmission zeroes," *IEEE Sensors Journal*, Vol. 17, No. 4, 994–999, 2017.